Effects of rare-earth element, Y, additions on the microstructure and mechanical properties of CoCrFeNi high entropy alloy

L.J. Zhang, M.D. Zhang, Z. Zhou, J.T. Fan, P. Cui, P.F. Yu, Q. Jing, M.Z. Ma, P.K. Liaw, G. Li, R.P. Liu

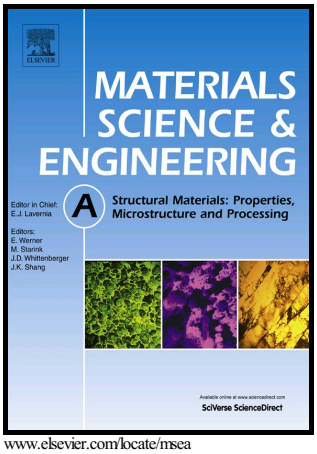

www.elsevier.com/locate/msea

PII: S0921-5093(18)30554-9
DOI: https://doi.org/10.1016/j.msea.2018.04.058
Reference: MSA36378

To appear in: *Materials Science & Engineering A*

Received date: 12 January 2018
Revised date: 8 April 2018
Accepted date: 12 April 2018

Cite this article as: L.J. Zhang, M.D. Zhang, Z. Zhou, J.T. Fan, P. Cui, P.F. Yu, Q. Jing, M.Z. Ma, P.K. Liaw, G. Li and R.P. Liu, Effects of rare-earth element, Y, additions on the microstructure and mechanical properties of CoCrFeNi high entropy alloy, *Materials Science & Engineering A*, https://doi.org/10.1016/j.msea.2018.04.058

Effects of rare-earth element, Y, additions on the microstructure and mechanical properties of CoCrFeNi high entropy alloy

L. J. Zhang[1], M. D. Zhang[1], Z. Zhou[1], J. T. Fan[1], P. Cui[1], P. F. Yu[1], Q. Jing[1], M. Z. Ma[1], P. K. Liaw[2], G. Li[1,2*], R. P. Liu[1*]

[1]State Key Laboratory of Metastable Materials Science and Technology, Yanshan University, Qinhuangdao 066004, China

[2]Department of Materials Science and Engineering, The University of Tennessee, Knoxville, TN 37996, USA

gongli@ysu.edu.cn

riping@ysu.edu.cn

Abstract

The effects of rare-earth element, Y, additions on the microstructures and mechanical properties of CoCrFeNi alloy have been investigated. The new series of $CoCrFeNiY_x$ (x = 0, 0.05, 0.1, 0.2, and 0.3) high entropy alloys were synthesized by vacuum arc-melting method. Microstructure characterizations were performed by the means of X-ray diffraction, scanning electron microscope, and transmission electron microscope. It was found that alloying Y element could lead to the formation of a simple hexagonal structure phase ($CaCu_5$ type). And another Ni_3Y-type hexagonal structure phase was observed in the alloy with higher Y contents (0.3 at.%). The phase evolution of the present alloy system was evaluated using the previous criteria ($\Delta H_{mix} - \delta$, $\Omega - \delta$, $\Delta\chi$, VEC, and Λ). The results of the nanoindentation measurements on different phases indicated that the hexagonal structure phases (~ 10.5 GPa) had a higher nanohardness than the face-centered cubic phase (~ 3 GPa). Furthermore, the maximum shear stress of the incipient plasticity was calculated to be 3.2 GPa for the face-centered cubic phase and 5.2 GPa for the hexagonal structure phase. The dislocation nucleation under the indenter in different phases was also discussed. The Vickers hardness and yield strength increased with increasing the Y content, while the fracture strength and plastic strain decreased. The strengthening mechanisms of the present alloys included solid-solution strengthening and the second

phase strengthening. Fracture surface observations suggested a ductile fracture in the face-centered cubic phase and a cleavage fracture in the hexagonal structure phase for the alloys containing Y element. The results of this investigation can provide a guide for the design of new high entropy alloy system with excellent properties.

Keywords: High-entropy alloy; Rare-earth element; Microstructure; Mechanical properties; Nanoindentation

1. Introduction

The design of metallic materials plays a crucial role in the development of human society and technology. For example, after the Stone Age, the emergence of subsequent ages (i.e., Bronze, Iron, and Steel) was closely related with the development of new materials. The copper alloys were replaced by the steel materials with superior combinations of strength and toughness. The steel materials are widely used in daily life, construction, transportation, and weapons, which have greatly contributed to the development of society. The most commonly used ferroalloys, titanium alloys, and aluminum alloys are all designed according to the traditional strategy based on one principal element (as solvent) with minor alloying additions (as solute) to obtain desired properties. After extensive and in-depth research, the development of these traditional alloys is approaching to the limit. For example, the principles of manufacturing and the classification of ferroalloys as well as their use were systematically summarized in [1]. Based on the one principal metal element strategy, approximately 30 alloy systems were developed and commercialized [2], such as high-speed steels, Stellite alloys, superalloys, stainless steels, alnico alloys, and Cu-Be alloys. In recent years, the high entropy alloys (HEAs) have been successfully developed under the guidance of a new alloy design concept. The HEAs were defined as the multi-component solid solution alloys with equimolar or near-equimolar compositions [3]. Due to the unique four core effects [3, 4]: high-entropy effects, sluggish diffusion, severe lattice distortion, and cocktail effects, the HEAs show many excellent properties, such as superb specific strength [4], superior mechanical performance at elevated temperatures [5], good fatigue [6, 7], oxidation and corrosion resistance [8, 9], and radiation tolerance [10]. With the

exceptional ductility and fracture toughness at cryogenic temperatures [5, 11], the single face-centered cubic (FCC) HEAs have attracted much attention. In order to improve the strength of the FCC HEAs, researchers have carried out various reinforcement methods [12-16]. For example, the high strength nanocrystalline FCC HEAs (CoCrFeNi and CoCrFeMnNi) have been fabricated by powder metallurgy [12, 13], equal-channel angular pressing [14], and high-pressure torsion [15, 16]. The powder metallurgy technique can ensure the structural refinement and homogeneous mixing of participating elements for HEAs. The large nanocrystalline or ultra-fine grained bulk samples can be obtained through the equal-channel angular pressing. The high-pressure torsion can produce high equivalent strain and lead to grain refinement and the significant increase in strength, such as the high strength to ~ 1.75 GPa for the CoCrFeNiMn HEA [15]. Through adjusting the content of Nb [17], Zr [18], and Ta [19] elements, the $CoCrFeNiNb_{0.65}$, $CoCrFeNiZr_{0.5}$, and $CoCrFeNiTa_{0.4}$ eutectic HEAs were prepared with modulated lamellar structures and excellent mechanical properties. For the $CoCrFeNiNb_{0.65}$ HEA, the eutectic structure was stable and the compressive fracture strengths were all above 2000 MPa at elevated temperatures between 600 °C and 900 °C [17]. The ultimate tensile strength of the $CoCrFeNiZr_{0.5}$ HEA was 450 MPa at the temperature of 650 °C [18]. The $CoCrFeNiTa_{0.4}$ HEA was found to have the high compression strength (2293 MPa) and relatively high plastic strain (22.6%) [19]. The precipitation-hardening behaviors have been studied for the FCC type HEAs by alloying with Al [20], Al/Ti [21], Ti [22], V [23], Mo [24], and Si [25] additions. However, the effects of rare-earth (RE) elements on the microstructure and mechanical properties of FCC type HEAs are still not clear. So far, there are very few articles on this topic [26].

With excellent physical and chemical properties, the RE elements, known as "industrial vitamins", play a huge role in improving product performance and increasing production efficiency. Additions of RE elements into steels have been an effective method extensively used to tailor microstructure and improve mechanical performance of the steels, owning to their positive effects on purification of molten steel and modification of inclusions [27, 28]. By the additions of 0.2 wt% RE

elements containing 65 wt% Ce and 35 wt% La, the tensile strength, yield strength, elongation, and hardness of the modified A357 alloy increased 15.4%, 4.5%, 6.3%, and 25.9% in as-cast condition because the RE elements could fine the α-Al primary phase and the eutectic silicon particles [29]. The formation of the thermally stable Al_4RE or $Al_{11}RE_3$ compounds can improve the high-temperature strength and creep resistance of the AZ91 magnesium alloy [30]. Therefore, alloying RE elements is a practical and effective method to optimize the mechanical properties of metallic materials. This method may be used in the HEAs to obtain superior mechanical properties. The purpose of the present work is to investigate the effects of RE element Y on the microstructural evolution and mechanical properties of the CoCrFeNi HEA. There are several reasons for our choice. Firstly, the excellent working hardening ability made the single FCC CoCrFeNi HEA an excellent base to further strengthen. Secondly, the new second-phase particles containing Y can be the dominant hardening factor of the CoCrFeNi HEA, owning to that the RE element Y is the hexagonal close-packed (HCP) structure stabilizer [31]. Thirdly, it is necessary to intensive study the phase evolution mechanism and the mechanical properties of the $CoCrFeNiY_x$ HEAs, for the low negative mixing enthalpy and high radius difference between Y and the constituent elements.

In order to clarify the detailed mechanical mechanism, the specific properties of the individual phase should be characterized exactly. The nanoindentation technique has made it possible to probe the local mechanical properties of different phases. Many previous studies [32-34] have applied this technique to analyze the elastic and plastic behaviors of different phases, such as nickel-based superalloy [32], $AlCrCuFeNi_2$ HEA [33], $Al_xCoCrCuFeNi$ (x = 0.5, 1.5 and 3.0) HEAs [34], and so on. In the present work, we performed detailed nanoindentation measurements on the different phases of the $CoCrFeNiY_x$ HEAs. The nanohardness and Young's modulus of the different phases were obtained. Moreover, the incipient plasticity on different phases was analyzed by measuring the first pop-in behavior. The precise characterization of the phase selection and the macro- and nano-mechanical properties of the $CoCrFeNiY_x$ HEAs can shed light on the design of new HEA system with

desired performance.

2. Experimental procedure

The ingots of $CoCrFeNiY_x$ (x = 0, 0.05, 0.1, 0.2, and 0.3) HEAs (denoted as Y_0, $Y_{0.05}$, $Y_{0.1}$, $Y_{0.2}$, and $Y_{0.3}$, respectively) were prepared by arc-melting a mixture of pure metals (purity > 99 wt.%) in a vacuum arc melting furnace with a water-cooled Cu crucible under a Ti-gettered high-purity argon atmosphere. During the melting process, these ingots were re-melted at least six times to guarantee compositional homogeneity. The crystal structure, microstructure, and phase composition of the present alloys were identified by X-ray diffraction (XRD), scanning electron microscope (SEM), and transmission electron microscopy (TEM) measurements. The XRD analysis was performed, using a D/MAX-2500/PC diffractometer with Cu Ka radiation (λ=1.54Å) scanning from 20° to 100° with a scanning rate of 4°/min. The ingot cross-sections for SEM observations were prepared by fine grinding with silicon carbide paper to grade 4000 followed by polishing using diamond paste. Then, the polished surfaces were etched with the aqua-regia solution (a mixture formed by freshly-mixing the concentrated nitric acid and hydrochloric acid usually in a volume ratio of 1:3). SEM investigations were performed using a Hitachi S-3400 scanning electron microscope (SEM) equipped with an energy-dispersive X-ray spectrometer (EDS). The spot measurements and EDS images were acquired to check the chemical compositions of different phases. The volume fraction of different phases was evaluated based on the measured area (in pixels) of the SEM images, using the ImageJ software. TEM samples were prepared by mechanical grinding to a thickness of less than 20 μm and further thinning was done using a Precision Ion Polisher (Gatan 695.B). The TEM observations were performed using a JEM-2100 apparatus at an accelerating voltage of 200 kV.

The Vickers hardness of the present HEAs was measured under a load of 500g for 15 s, using a hardness tester (HVS-1000). Tensile tests were performed using an INSTRON-5982 materials testing machine at a strain rate of 1×10^{-3} s^{-1} at room temperatures. The dog-bone-shaped tensile specimens had a gauge section of 8 mm (l) × 2 mm (w) × 1 mm (t). The cylindrical specimens with the size of 3 mm in diameter

and 6 mm in length were cut for the room-temperature compression tests using an INSTRON-5982 machine under a strain rate of 5×10^{-4} s^{-1}. For each specimen, at least 3 measurements were carried out to ensure the accuracy of the data.

The nanoindentation experiments were conducted at room temperature, using a Hysitron Triboindenter (TI-900) equipped with a Berkovich diamond tip. The effective tip radius of the Berkovich indenter was determined from the calibration tests on the single-crystal tungsten to be 400 nm. We should keep that the sample surface must be polished to a mirror of 10 nm for the nanoindentation measurements. The position of the two different phases can be determined through the optical microscope equipped on the Triboindenter. The samples were loaded to a maximum load of 5,000 μN under the constant loading rate of 1,000 μN s^{-1} with a fixed holding time of 2 s, followed by unloading to zero to measure the nanohardness and Young's modulus on different phases. The incipient plasticity behavior was probed by measuring the first pop-in behavior in the loading segment of the load-displacement (*P-h*) curve at a loading rate of 50 μN s^{-1} to 1,000 μN. The nanoindentation measurements were carried out when the thermal drift < 0.05 nm/s in every experiment. In order to ensure the accuracy of measurement results, more than 10 tests were performed for each condition.

3. Results

3.1 Crystal structure and microstructures

Fig. 1(a) shows the XRD profiles of the $CoCrFeNiY_x$ (x = 0, 0.05, 0.1, 0.2, and 0.3) HEAs. The FCC phase exists in each sample, as can be seen from the $(111)_{FCC}$ reflection. The new reflection peaks corresponding to a simple hexagonal structure (HS1) phase can be obviously observed in the $Y_{0.05}$, $Y_{0.1}$, $Y_{0.2}$, and $Y_{0.3}$ alloys. The space group of the HS1 phase was identified as P_6/mmm ($CaCu_5$ type), which agrees well with our previous reports [26]. However, for the $Y_{0.3}$ alloy, another hexagonal structure (HS2) phase was detected with the space group P_{63}/mmc (Ni_3Y type), as shown in Fig. 1(a) and (b). The enhancement of the peak intensity suggested that the volume fraction of the HS1 phase increased with increasing the Y concentration. Moreover, the $(111)_{FCC}$ peak of the FCC phase shifts towards a lower 2θ angle as the

Y content increases (shown in Fig. 1(b)), which implies that the lattice parameters increase. The calculated lattice parameters of the FCC phase are shown in Fig. 1(c). The dissolution of the RE element Y with a larger atomic radius than other constituent elements (see Table 1) led to severe lattice distortion, which was the main reason resulting in the increase of the lattice parameters.

The SEM images of the $CoCrFeNiY_x$ HEAs with different Y contents are shown in Fig. 2. The CoCrFeNi base alloy is the single FCC structure with the average grain size of ~ 200 μm, as shown in Fig. 2(a). By adding RE element Y, the alloy morphology becomes the dendrite (DR) and interdendrite (ID) structure for the $Y_{0.05}$, $Y_{0.1}$, $Y_{0.2}$, and $Y_{0.3}$ alloys. The DR area structure is FCC phase, and the ID area structure is HS1 phase for the $Y_{0.05}$, $Y_{0.1}$, and $Y_{0.2}$ alloys, as shown in Fig. 2(b)-(d). While for the $Y_{0.3}$ alloy (Fig. 2(e)), the ID region contains HS1 phase and HS2 phase, respectively. As seen in Fig. 2(f), the volume fraction of the HS phase (ID area) increases from 14.6% ($Y_{0.05}$ alloy) to 52.2% ($Y_{0.3}$ alloy) accordingly. To identify the phase compositions of the different phases in the $CoCrFeNiY_x$ HEAs, we performed EDS point analysis and the results were summarized in Table 2. One can note that the higher concentrations of Y and Ni in the HS1 phase and HS2 phase because of the negative mixing enthalpy of Y-Ni (see Table 1). The EDS images in Fig. 3 clearly display that the Co, Cr, and Fe elements are almost homogeneous in the FCC phase and a segregation Y and Ni concentration is in the HS1 phase for the $Y_{0.1}$ HEA. However, the content of Ni in the FCC phase shows a slight decrease, compared with other elements. The results are in agreement with the data in Table 2. TEM observations were carried out for the $Y_{0.1}$ HEA to further research the microstructure. The typical bright field TEM image and corresponding selected area electron diffraction (SAED) patterns of ID and DR in the $Y_{0.1}$ alloy are presented in Fig. 4. The [011] zone axis SAED [Fig. 4(b)] of the white area verifies that it is a FCC phase. Fig. 4(c) shows the SAED pattern taken along the $[1\bar{2}1\bar{3}]$ zone axis of the dark area with hexagonal structure. The SAED patterns further confirmed that the $Y_{0.1}$ alloy consisted of a FCC phase and a $CaCu_5$ type HS1 phase.

3.2 Nano-mechanical properties tests

The crystal structure and morphology of the $CoCrFeNiY_x$ HEAs have been identified. Next, it is necessary to study the mechanical performance and the strengthening mechanism of the FCC and HS phases. The nanoindentation method is the easy-to-use and effective method to investigate the nano-mechanical properties and deformation behavior in a small volume of materials, such as small grain with different grain orientation [35] and individual phases [36]. The influence of the grain boundary and the grain orientation should be noticed during nanoindentation tests. The indentation in the center of every phase and the small indentaion size (the maximum penetration depth of < 220 nm (Fig. 5(a)), the maximum width < 3 μm) under the maximum load of 5,000 μN can keep the plastic zone size smaller than the size of individual phases (> 10 μm (Fig. 2)). In the present alloy system, the different crystal structures can influence the nanoindentation results to a much greater degree than the different grain orientations. Chen et al. [35] have pointed out that the dependence of nanohardness on grain orientation was not strong for the single FCC Fe-20Cr-25Ni alloy. The statistic nanohardness distributions of the indentations close to {001}, {101}, and {111} were from 1.85 to 2.21 GPa. Our previous paper [26] suggested that the $CaCu_5$ type HS phase was a brittle phase and the nanohardness was almost three times that of the FCC phase. In the present study, we focus on the differences in mechanical properties on different phases. Therefore, the influences from the grain boundary and the grain orientation can be negligible in our present work.

Fig. 5(a) presents the typical nanoindentation *P-h* curves of the FCC and HS1 phases in the $Y_{0.2}$ HEA. It is obvious that the maximum penetration depth in the FCC phase is greater than that in the HS1 phase under the same maximum load, indicating that the HS1 phase is more resistant to plastic deformation. The nanohardness and Young's modulus on the different phases of $CoCrFeNiY_x$ HEAs are extracted from the *P-h* curves based on the Oliver-Pharr method [37]. As shown in Fig. 5(b), it can be found that the nanohardness of the FCC phase increases from 2.9 GPa (Y_0 alloy) to 3.3 GPa ($Y_{0.3}$ alloy) and the HS1 and HS2 phases have the same value of ~ 10.5 GPa.

The nanohardness of the FCC phase in $Y_{0.3}$ alloy was 13.8% higher than that of the Y_0 alloy. However, the change of Young's modulus is not so obvious with the Y content increasing, as shown in Fig. 5(c). The Young's modulus values of the HS1 and HS2 phases are almost the same (~ 215 GPa), which is ~ 25 GPa higher than that of the FCC phase (~ 190 GPa). In order to investigate the incipient plasticity of the different phases, the first pop-in behavior was detected by measuring the first displacement burst in the *P-h* curves, as shown in Fig. 6(a). The values of the maximum shear stress on different phases for the elastic-to-plastic transition were calculated depending on the first pop-in load and depth, as shown in Fig. 6(b). The strengthening mechanism and deformation behavior taking place in the FCC phase and HS phase will be discussed in the following section.

3.3 Macro-mechanical properties measurements

Fig. 7 shows the variation of the Vickers hardness of the $CoCrFeNiY_x$ HEAs. With increasing the Y content, the Vickers hardness values increase from 146 HV (Y_0 alloy) to 400 HV (the $Y_{0.3}$ alloy). As shown in Fig. 2, it is obvious that the increasing of the RE element Y content accompanies with the volume fraction increase of the HS phase. Roughly, the relationship between the Vickers hardness and the HS phase volume fraction can be expressed as $HV = 1.01679V_{HS}^{1.38} + 148.09$, where HV is the Vickers hardness value, and V_{HS} is the volume fraction of the HS phase (vol.%), when the content of RE element Y does not exceed 0.3 (at.%). The increase of the volume fraction of the hard HS phase can result in the increase of the Vickers hardness.

The tensile engineering stress-strain curves for the current $CoCrFeNiY_x$ HEAs containing different amounts of RE element Y are depicted in Fig. 8(a). The addition of the Y element results in the embrittlement of the current alloy system for the tensile testing, especially for the $Y_{0.1}$, $Y_{0.2}$, and $Y_{0.3}$ alloys. The same results can be observed in the $CoCrFeNiZr_x$ HEAs system [18]. The room temperature compressive engineering stress–strain curves are shown in Fig. 8(b). The summary of the compression yield strength, σ_y, fracture strength, σ_f, and plastic strain, ε_p, as a

function of the RE element Y content are listed in Table 3. The Y_0 alloy exhibits the low yield strength of 202 MPa and high working hardening ability with compressing to 60% height reduction without fracture. With increasing x value of the $CoCrFeNiY_x$ HEAs, the yield strength increases, while the fracture strength and plastic strain decrease. The yield strength increases from 563 MPa ($Y_{0.05}$ alloy) to 1,440 MPa ($Y_{0.3}$ alloy). The fracture strength and plastic strain of the $Y_{0.05}$ alloy are 2,175 MPa and 33.5%, respectively, but reduce appreciably to 1,605 MPa and 2.3%, respectively, in the $Y_{0.3}$ alloy. The yield strength as a function of the volume fraction of the HS phase is shown in Fig. 8(c). The macro-mechanical properties are closely related with the phase boundaries and the mechanical properties of the different phases. Nanoindentation measurements revealed that the HS phases had a high nanohardness of ~ 10.5 GPa, which was the main strengthening factor for the current HEAs.

The fracture morphologies of the $CoCrFeNiY_x$ HEAs are shown in Fig. 9. The large dimples can be observed in the Y_0 alloy fracture surface [see Fig. 9(a)]. While the $Y_{0.05}$, $Y_{0.1}$, $Y_{0.2}$, and $Y_{0.3}$ alloys contain the brittle and ductile fracture regions [see Fig. 9(b)-(f)]. The brittle region shows the cleavage fracture. The ductile fracture region is FCC phase. With the increase of the volume fraction of HS phase, the fracture mode of the alloys changed from ductile fracture to brittle fracture. The strengthening and fracture mechanisms will be discussed in the next section.

4. Discussion

4.1 Phase formation

In order to predict the phase formation, researchers have proposed a couple of criteria based on the compositions of the multi-component HEAs. Two effective criteria, $\Delta H_{mix} - \delta$ and $\Omega - \delta$, have been suggested by Zhang [38] and Yang [39] according to the thermodynamics and geometry effects. The corresponding physical parameters are expressed as follows:

$$\Delta H_{mix} = \sum_{i=1, i\neq j}^{n} \Omega_{ij} c_i c_j \quad (1)$$

$$\Delta S_{mix} = -R\sum_{i=1}^{n}(c_i \ln c_i) \quad (2)$$

$$\Omega = \frac{T_m \Delta S_{mix}}{|\Delta H_{mix}|} \quad (3)$$

$$T_m = \sum_{i=1}^{n} c_i (T_m)_i \quad (4)$$

$$\delta = \sqrt{\sum_{i=1}^{n} c_i (1 - \frac{r_i}{\bar{r}})^2} \quad (5)$$

where, c_i and c_j is the atomic percent of the *i*th the *j*th element; $\Omega_{ij} = (4\Delta H_{AB}^{mix})$ is the regular solution-interaction parameter between the *i*th and *j*th components, ΔH_{AB}^{mix} is the mixing enthalpy between the *i*th and *j*th elements, calculated by the Miedema's approach [40]; ΔS_{mix} is the mixing entropy of an n-component HEA, R is the gas constant; $(T_m)_i$ is the melting point of the *i*th constituent element (see Table 1); δ is the atomic size mismatch; $\bar{r} = \sum_{i=1}^{n} c_i r_i$ is the average atomic radius, and r_i is the atomic radius of the *i*th component (see Table 1). The two regions for the single solid solution formation are -15 < ΔH_{mix} < 5 kJ/mol, $\delta \le 6.6\%$ [38], and $\Omega \ge 1.1$, $\delta \le 6.6\%$ [39]. Beyond these regions, the intermetallic compounds and the amorphous phase have a chance to occur. For the current $CoCrFeNiY_x$ HEAs system, the calculated physical values of ΔS_{mix}, ΔH_{mix}, Ω, and δ were listed in Table 4. The $Y_{0.05}$ alloy had $\Delta H_{mix} = -4.181$ kJ/mol, $\delta = 4.879\%$, and $\Omega = 5.342$. According to the above criteria, the $Y_{0.05}$ alloy should fall into the single solid solution region. However, in the present work, the $Y_{0.05}$ alloy contains the FCC phase (solid solution) and the HS1 phase (intermetallic compounds). Therefore, the $\Delta H_{mix} - \delta$ and $\Omega - \delta$ criteria fail to predict the phase formation for the $CoCrFeNiY_x$ HEAs.

Recently, Yurchenko et al. has proposed a new criteria of $\delta > 5\%$ for predicting the Laves-phase formation after analyzing approximately 150 different HEAs [41]. It can be seen in Table 4 that the formation of the HS1 phase is observed

in the range of $\delta > 4.8\%$, which is very close to the Laves-phase formation range. What's more, the HS1 phase structure ($CaCu_5$ type) can be obtained from the C14 and C15 Laves-phase structure [42]. The HS1 phase is closely related to the Laves-phase. Thus, the range of $\delta > 4.8\%$ can be used for predicting the HS1 phase formation.

In addition to the criteria mentioned above, researchers also put forward other criteria. For example, the electro-negativity difference ($\Delta\chi = \sqrt{\sum_{i=1}^{n} c_i(\chi_i - \bar{\chi})^2}$, where χ_i is the Pauling electro-negativity for the *i*th component, and $\bar{\chi} = \sum_{i=1}^{n} c_i\chi_i$ is the average Pauling electro-negativity) has been used to predict the formation of the topologically close-packed (TCP) phase of HEAs when $\Delta\chi > 0.133$ [43]. However, the boundary of the HS1 phase formation is $\Delta\chi > 0.11$ for the present $CoCrFeNiY_x$ HEAs, as shown in Table 4. According to the valence-electron concentration (VEC) criteria, the FCC phases are stable at higher VEC$\geq$8 and instead bcc phases are stable at lower VEC<6.87. The $Y_{0.05}$, $Y_{0.1}$, and $Y_{0.2}$ alloys have VEC$\geq$8 (see Table 4) and should fall into the single FCC zone from the VEC criteria. However, these alloys contain the FCC and HS1 phases. So the VEC criterion is invalid for the $CoCrFeNiY_x$ alloy system. The geometrical parameter ($\Lambda = \Delta S_{mix}/\delta^2$) was proposed by Singh [44]. There are three ranges for the Λ-parameter: (1) only compound(s) ($\Lambda < 0.24$), (2) a mixture involving compounds ($0.24 < \Lambda < 0.96$), and (3) disordered solid solutions ($\Lambda > 0.96$). According to the Λ-parameter, the $Y_{0.2}$ and $Y_{0.3}$ alloys ($\Lambda < 0.16$) (see Table 3) should fall into the only intermetallic compounds zone. However, the FCC solid solution phase in the two alloys suggested that the Λ-parameter criterion also failed to predict the phase formation of the present Y-containing HEA system.

4.2 The incipient plasticity behavior on the FCC and HS1 phases

Instrumented nanoindentation has been an effective and successful method to detect the onset of yielding in crystals with small size. The plastic yielding behavior is associated with the distinct displacements, which are often referred as pop-ins, in the *P-h* curve. The first pop-in behavior is attributed to the nucleation and/or activation of dislocation, which is often observed when the shear-stresses underneath

the indenter approach theoretical limits of G/30 - G/5, where G is the shear modulus [45, 46]. In the present work, nanoindentation tests were carried out to measure the first pop-in behavior of the FCC phase and HS1 phase in order to investigate the effects of the crystal structure on the incipient plasticity behavior. The first pop-in occurring in the loading segment of a *P*-*h* curve represents an elastic-to-plastic transition, as shown in Fig. 6(a). Before the first pop-in event, the deformation is the purely elastic deformation, which can be described well by the Hertzian elastic theory [47]:

$$P = \frac{4}{3} E_r R^{1/2} h^{3/2} \tag{6}$$

where P is the indentation load, R is the tip radius of the indenter, h is indentation depth, and $E_r = \left[(1 - \nu_i^2)/E_i + (1 - \nu_s^2)/E_s \right]^{-1}$ is the reduced modulus, where ν_i (= 0.07) and E_i (= 1,141 GPa) are the Poisson's ratio and Young's modulus of the indenter, ν_s and E_s are the Poisson's ratio and Young's modulus of the specimen, respectively. The well Hertzian fitting for the *P*-*h* curves was shown in Fig. 6(a), which gave the fitting coefficient of 2.91 and 5.35 for the FCC phase and HS1 phase. The reduced modulus can be calculated from the fitting coefficient. Based on Equation (6), the HS1 phase had the higher value of reduced modulus than that of FCC phase. The corresponding average reduced modulus on different phases was shown in Fig. 6(b).

During nanoindentation, the shear stress underneath the indenter at the onset of the first pop-in was assumed to be the maximum shear stress, τ_{max}, which was expressed as [47]:

$$\tau_{\max} = 0.31 \left(\frac{6 E_r^2}{\pi^3 R^2} P \right)^{\frac{1}{3}} \tag{7}$$

As can be seen in Fig. 5(b), the average value of τ_{max} for the FCC phase is obtained as ~ 3.2 GPa (G_F/23), where G_F (~ 73 GPa, estimated from the Young's modulus and a Poisson's ratio of 0.3) is the shear modulus of the FCC phase. The τ_{max} on the HS1 phase is about 5.2 GPa (G_H/15), where G_H (~ 82 GPa) is the shear modulus of the

HS1 phase. Many researchers [48-51] have studied the dislocation nucleation underneath the indenter for different materials with varying crystal structures. Through measuring the first pop-in behavior, Ye and Wang et al. have concluded that the full dislocation nucleation was favored in the BCC metals (e.g., Mo [48] and TiZrHfNb [49]) with the higher activation energy, whereas the partial dislocation nucleation was favored in FCC metals (e.g., Ni [48] and CoCrFeNiMn [49]) with the lower activation energy. Catoor et al. [50] have founded that the first pop-in behavior of the HCP Mg single crystal was due to the homogeneous nucleation of full dislocations in all three orientations, and the shear stresses fall in the range of G/30 - G/14. During the first pop-in event, the dislocation nucleation under the indenter was treated as a stress-assisted, thermally-activated process [51]. For the present alloy, the dislocation nucleation for the FCC phase can occur more easily with a lower τ_{max} (G_F/23) than the HS1 phase with a higher τ_{max} (G_H/15). The partial dislocations can be triggered in the FCC phase with the lower activation energy, and the full dislocations can be triggered in the HS1 phase with the higher activation energy. Moreover, the large atomic-size difference between the RE element Y and other constituent components can lead to the higher activation energy of dislocation nucleation.

4.3 The strengthening mechanisms analysis

The addition of the RE element Y can significantly improve the hardness or strength because of the formation of the hard HS phase for the $CoCrFeNiY_x$ HEAs, as shown in Figs. 7 and 8. The strengthening mechanisms in the present alloys are traditionally summarized into two categories: solid-solution strengthening and the second phase strengthening. For the FCC phase in the alloys with different Y content, the nanohardness slightly increased from 2.9 GPa (Y_0 alloy) to 3.3 GPa ($Y_{0.3}$ alloy) (Fig. 5), suggesting a solution strengthening effect caused by the enlarged lattice distortion. The FCC solid solution phase was simply treated as a CoCrFeNi solvent matrix containing Y solutes. Here, the potency of the solution strengthening caused by Y was evaluated by a standard model for substitutional solid solution strengthening based on the dislocation-solute elastic interactions [52]:

$$\Delta H = 3^{3/2} \cdot \frac{G \cdot \varepsilon_s^{3/2} \cdot c^{1/2}}{700} \quad (8)$$

where G is the shear modulus of CoCrFeNi obtained using the equation $G=E/2(1+v)$, E is the Young's modulus by nanoindentation tests. v is Poisson's ratio taken as v = 0.3, c is the molar ratio of Y element, $3^{3/2}$ is an approximate conversion factor from shear stress to hardness. The interaction parameter ε_s can be expressed as:

$$\varepsilon_s = \left| \frac{\varepsilon_G}{1+0.5\varepsilon_G} - 3 \cdot \varepsilon_\alpha \right| \quad (9)$$

which combines the elastic and atomic size mismatche, i.e. ε_G and ε_α, and they are defined as:

$$\varepsilon_G = \frac{1}{G}\frac{\partial G}{\partial c} \quad (10)$$

$$\varepsilon_\alpha = \frac{1}{\alpha}\frac{\partial \alpha}{\partial c} \quad (11)$$

where α is the lattice constant of CoCrFeNi. The atomic size mismatche ε_α can be obtained from Fig. 1(c). However, the parameter ε_G is usually negligible compared with ε_α. In this case, the value of ε_s and thus ΔH can be readily calculated. As for the FCC phase in the $Y_{0.3}$ alloy, the strength increment caused by the solid-solution strengthening was estimated to be 27.1 MPa. It is noted that the calculated increment in hardness is smaller compared with the nanoindentation results [34] (Fig. 5). The similar results could be observed for the FCC phase in the Al_xCoCrCuFeNi (x = 0.5, 1.5 and 3.0) alloys with the solid-solution strengthening effect of the Al increment [34]. The indentation size effect (ISE) [53] of the nanoindentation method can contribute to the increase of the observed nanohardness with the small penetration depth of ~ 210 nm.

The second phase strengthening of the HS phase was the main strengthening mechanism of the CoCrFeNiY_x HEAs. The hardness and strength were improved with the increase in volume fraction of the HS phase (Figs. 7 and 8). The nanoindentation results indicated that the HS phase was more brittle but stronger than the FCC phase because of the difference in the number of their available slip systems (Fig. 5). To the first approximation, the strength of the current alloys can be described

by the simple rule-of-mixture [20]:

$$\sigma_y = \sigma_{FCC} V_{FCC} + \sigma_{HS} V_{HS} \quad (12)$$

where σ_{FCC} and σ_{HS} are the yield strength of the FCC phase and HS phase, V_{FCC} and V_{HS} are the volume fraction. We must point out that the "HS phase" represent HS1 phase for the $Y_{0.05}$, $Y_{0.1}$, and $Y_{0.2}$ alloys and HS1+HS2 phases for the $Y_{0.3}$ alloy, because the HS1 and HS2 phases have the same hardness or strength (Fig. 5). Considering the $V_{FCC} + V_{HS} = 1$, Equation (12) can be converted to:

$$\sigma_y = \sigma_{FCC} + (\sigma_{HS} - \sigma_{FCC}) V_{HS} \quad (13)$$

Consequently, a good linear relationship for the yield strength as a function of V_{HS} was observed in Fig. 8(c). The well fitting curve indicated that the traditional composite model could offer reasonable interpretation for the yield strength increment of the $CoCrFeNiY_x$ HEAs.

4.4 Fracture mechanisms analysis

Fig. 9 shows the fracture surface morphology to further understand the relationship between the structure and the mechanical property as well as the fracture mechanism of the $CoCrFeNiY_x$ alloys. The fracture structure of the Y_0 alloy is the typical ductile fracture with the large dimples, suggesting an excellent plasticity for the alloy, as shown in Fig. 9(a). Two different kinds of fracture modes can be clearly distinguished for the FCC and HS phases in $Y_{0.05}$, $Y_{0.1}$, $Y_{0.2}$, and $Y_{0.3}$ alloys [Fig. 9(b)-(f)]. The cleavage fracture can be observed for the HS phase. However, the FCC phase is subjected to an excellent plastic deformation by necking into sharp lines without any dimples. Obvious cracks lay at the phase boundaries, indicating that the cracks first nucleated at the FCC and HS phase boundaries due to stress concentration and then propagated in the HS phase. Especially for the $Y_{0.3}$ alloy with the high volume fraction of the HS phase (52.2 %), the continuous HS phase will contribute to the rapid expansion of the crack, which leads to the decrease of the fracture strength.

5. Conclusions

In this work, microstructure and mechanical properties of the $CoCrFeNiY_x$ (x =

0, 0.05, 0.1, 0.2, and 0.3) HEAs were examined in as-cast condition. The main conclusions were as follows:

(1) The additions of the RE element Y into the CoCrFeNi HEA changed the original single FCC phase structure to the dendrite structure and led to the formation of a new HS1 phase ($CaCu_5$ type). With further improving the Y content, another new HS2 phase (Ni_3Y type) was observed in the $Y_{0.3}$ alloy.

(2) The previous criteria ($\Delta H_{mix} - \delta$, $\Omega - \delta$, $\Delta\chi$, VEC, and Λ) cannot effectively predict the phases formation of the present $CoCrFeNiY_x$ HEAs. Based on our analyses, the new intermetallic compounds (HS1 phase) can form when $\delta > 4.8\%$ and $\Delta\chi > 0.11$.

(3) Nanoindentation tests indicated that the nanohardness of the FCC phase showed a slight increase from 2.9 GPa (Y_0 alloy) to 3.3 GPa ($Y_{0.3}$ alloy), while the HS1 and HS2 phases had the same value of ~ 10.5 GPa. The values of the maximum shear stress during the first pop-in event were 3.2 GPa for the FCC phase and 5.2 GPa for the HS1 phase.

(4) The minor addition of RE element Y significantly increased the Vickers hardness from 146 HV (Y_0 alloy) to 400 HV ($Y_{0.3}$ alloy) and the yield strength from 202 MPa (Y_0 alloy) to 1,440 MPa ($Y_{0.3}$ alloy). The strengthening mechanisms contain solid-solution strengthening and the second phase strengthening.

(5) A ductile fracture in the FCC phase and a cleavage fracture in the HS phase were found in the alloys containing Y element. The cracks nucleated at the phase boundaries by stress concentration and could easily propagate in the HS phase. The increase of the brittle HS phase volume fraction resulted in the decrease of the fracture strength for the present alloy system.

Acknowledgments

Gong Li would like to acknowledge the Basic Research Project in the Hebei Province (Grant No. A2016203382), and the support from the National Science

Foundation of China (Grant No. 11674274). Peng Fei Yu would like to acknowledge the National Natural Science Funds of China (Grant No. 51601166), and the Research Program of the College Science & Technology of the Hebei Province (Grant No. QN2016167).

References

[1] R.H. Eric, Production of Ferroalloys, 2014.
[2] J.W. Yeh, Overview of High-Entropy Alloys, Springer International Publishing 2016.
[3] J.W. Yeh, Recent progress in high-entropy alloys, Ann Chim-Sci Mat 31(6) (2006) 633-648.
[4] Y. Zhang, T.T. Zuo, Z. Tang, M.C. Gao, K.A. Dahmen, P.K. Liaw, Z.P. Lu, Microstructures and properties of high-entropy alloys, Prog Mater Sci 61 (2014) 1-93.
[5] Y.F. Ye, Q. Wang, J. Lu, C.T. Liu, Y. Yang, High-entropy alloy: challenges and prospects, Materials Today 19(6) (2016) 349-362.
[6] M. Seifi, D. Li, Z. Yong, P.K. Liaw, J.J. Lewandowski, Fracture Toughness and Fatigue Crack Growth Behavior of As-Cast High-Entropy Alloys, JOM 67(10) (2015) 2288-2295.
[7] Z. Tang, T. Yuan, C.W. Tsai, J.W. Yeh, C.D. Lundin, P.K. Liaw, Fatigue behavior of a wrought $Al_{0.5}CoCrCuFeNi$ two-phase high-entropy alloy, Acta Materialia 99 (2015) 247-258.
[8] Y.L. Chou, Y.C. Wang, J.W. Yeh, H.C. Shih, Pitting corrosion of the high-entropy alloy $Co_{1.5}CrFeNi_{1.5}Ti_{0.5}Mo_{0.1}$ in chloride-containing sulphate solutions, Corros Sci 52(10) (2010) 3481-3491.
[9] M.H. Chuang, M.H. Tsai, W.R. Wang, S.J. Lin, J.W. Yeh, Microstructure and wear behavior of $Al_xCo_{1.5}CrFeNi_{1.5}Ti_y$ high-entropy alloys, Acta Materialia 59(16) (2011) 6308-6317.
[10] C. Lu, L. Niu, N. Chen, K. Jin, T. Yang, P. Xiu, Y. Zhang, F. Gao, H. Bei, S. Shi, Enhancing radiation tolerance by controlling defect mobility and migration pathways in multicomponent single-phase alloys, Nature Communications 7 (2016) 13564.
[11] B. Gludovatz, A. Hohenwarter, D. Catoor, E.H. Chang, E.P. George, R.O. Ritchie, A fracture-resistant high-entropy alloy for cryogenic applications, Science 345(6201) (2014) 1153.
[12] P. Sathiyamoorthi, J. Basu, S. Kashyap, K.G. Pradeep, R.S. Kottada, Thermal stability and grain boundary strengthening in ultrafine-grained CoCrFeNi high entropy alloy composite, Mater Design 134 (2017) 426–433.
[13] Y. Liu, J. Wang, Q. Fang, B. Liu, Y. Wu, S. Chen, Preparation of superfine-grained high entropy alloy by spark plasma sintering gas atomized powder, Intermetallics 68 (2016) 16-22.
[14] H. Shahmir, T. Mousavi, J. He, Z. Lu, M. Kawasaki, T.G. Langdon, Microstructure and properties of a CoCrFeNiMn high-entropy alloy processed by

equal-channel angular pressing, Materials Science and Engineering: A 705 (2017) 411–419..

[15] H. Shahmir, J. He, Z. Lu, M. Kawasaki, T.G. Langdon, Effect of annealing on mechanical properties of a nanocrystalline CoCrFeNiMn high-entropy alloy processed by high-pressure torsion, Materials Science & Engineering A 676 (2016) 294-303.

[16] B. Schuh, F. Mendez-Martin, B. Völker, E.P. George, H. Clemens, R. Pippan, A. Hohenwarter, Mechanical properties, microstructure and thermal stability of a nanocrystalline CoCrFeMnNi high-entropy alloy after severe plastic deformation, Acta Materialia 96 (2015) 258-268.

[17] F. He, Z. Wang, X. Shang, C. Leng, J. Li, J. Wang, Stability of lamellar structures in CoCrFeNiNb x eutectic high entropy alloys at elevated temperatures, Mater Design 104 (2016) 259-264.

[18] W. Huo, H. Zhou, F. Fang, Z. Xie, J. Jiang, Microstructure and mechanical properties of $CoCrFeNiZr_x$ eutectic high-entropy alloys, Mater Design 134 (2017) 226–233.

[19] H. Jiang, K. Han, D. Qiao, Y. Lu, Z. Cao, T. Li, Effects of Ta Addition on the Microstructures and Mechanical Properties of CoCrFeNi High Entropy Alloy, Materials Chemistry & Physics xxx (2017) 1-6.

[20] J.Y. He, W.H. Liu, H. Wang, Y. Wu, X.J. Liu, T.G. Nieh, Z.P. Lu, Effects of Al addition on structural evolution and tensile properties of the FeCoNiCrMn high-entropy alloy system, Acta Materialia 62(1) (2014) 105-113.

[21] J.Y. He, H. Wang, H.L. Huang, X.D. Xu, M.W. Chen, Y. Wu, X.J. Liu, T.G. Nieh, K. An, Z.P. Lu, A precipitation-hardened high-entropy alloy with outstanding tensile properties, Acta Materialia 102 (2016) 187-196.

[22] T.-T. Shun, L.-Y. Chang, M.-H. Shiu, Microstructures and mechanical properties of multiprincipal component $CoCrFeNiTi_x$ alloys, Materials Science and Engineering: A 556 (2012) 170-174.

[23] N.D. Stepanov, D.G. Shaysultanov, G.A. Salishchev, M.A. Tikhonovsky, E.E. Oleynik, A.S. Tortika, O.N. Senkov, Effect of V content on microstructure and mechanical properties of the $CoCrFeMnNiV_x$ high entropy alloys, Journal of Alloys & Compounds 628(628) (2015) 170-185.

[24] W.H. Liu, Z.P. Lu, J.Y. He, J.H. Luan, Z.J. Wang, B. Liu, Y. Liu, M.W. Chen, C.T. Liu, Ductile $CoCrFeNiMo_x$ high entropy alloys strengthened by hard intermetallic phases, Acta Materialia 116 (2016) 332-342.

[25] K.H. Kong, C.K. Kang, W.T. Kim, D.H. Kim, Microstructural Features of Multicomponent $FeCoCrNiSi_x$ Alloys, Applied Microscopy 45(1) (2015) 32-36.

[26] L.J. Zhang, P.F. Yu, M.D. Zhang, D.J. Liu, Z. Zhou, M.Z. Ma, P.K. Liaw, G. Li, R.P. Liu, Microstructure and mechanical behaviors of $Gd_xCoCrCuFeNi$ high-entropy alloys, Materials Science & Engineering A 707 (2017) 708-716.

[27] L.M. Wang, Q. Lin, L.J. Yue, L. Liu, F. Guo, F.M. Wang, Study of application of rare earth elements in advanced low alloy steels, Journal of Alloys & Compounds 451(1) (2008) 534-537.

[28] Y. Zhao, J. Wang, S. Zhou, X. Wang, Effects of rare earth addition on microstructure and mechanical properties of a Fe–15Mn–1.5Al–0.6C TWIP steel,

Materials Science & Engineering A 608(11) (2014) 106-113.
[29] W. Jiang, Z. Fan, Y. Dai, C. Li, Effects of rare earth elements addition on microstructures, tensile properties and fractography of A357 alloy, Materials Science & Engineering A 597(597) (2014) 237-244.
[30] F. Khomamizadeh, B. Nami, S. Khoshkhooei, Effect of rare-earth element additions on high-temperature mechanical properties of AZ91 magnesium alloy, Metallurgical & Materials Transactions A 36(12) (2005) 3489-3494.
[31] L. Guenee, K. Yvon, Structure stability maps for intermetallic AB(5) compounds, J Alloy Compd 356 (2003) 114-119.
[32] H.U. Rehman, K. Durst, S. Neumeier, A.B. Parsa, A. Kostka, G. Eggeler, M. Göken, Nanoindentation studies of the mechanical properties of the μ phase in a creep deformed Re containing nickel-based superalloy, Materials Science & Engineering A 634 (2015) 202-208.
[33] Y. Sun, G. Zhao, X. Wen, J. Qiao, F. Yang, Nanoindentation deformation of a bi-phase $AlCrCuFeNi_2$ alloy, Journal of Alloys & Compounds 608(5) (2014) 49-53.
[34] Y. Sun, P. Chen, L. Liu, M. Yan, X. Wu, C. Yu, Z. Liu, Local mechanical properties of $Al_xCoCrCuFeNi$ high entropy alloy characterized using nanoindentation, Intermetallics 93 (2018) 85-88.
[35] T. Chen, L. Tan, Z. Lu, H. Xu, The effect of grain orientation on nanoindentation behavior of model austenitic alloy Fe-20Cr-25Ni ☆, Acta Materialia 138 (2017) 83-91.
[36] H.U. Rehman, K. Durst, S. Neumeier, A.B. Parsa, A. Kostka, G. Eggeler, M. Goken, Nanoindentation studies of the mechanical properties of the mu phase in a creep deformed Re containing nickel-based superalloy, Mat Sci Eng a-Struct 634 (2015) 202-208.
[37] Oliver, W.C, Pharr, G.M, An improved technique for determining hardness and elastic modulus using load and displacement sensing indentation experiments, Journal of Materials Research 7(6) (1992) 1564-1583.
[38] Y. Zhang, Y.J. Zhou, J.P. Lin, G.L. Chen, P.K. Liaw, Solid-solution phase formation rules for multi-component alloys, Adv Eng Mater 10(6) (2008) 534-538.
[39] X. Yang, Y. Zhang, Prediction of high-entropy stabilized solid-solution in multi-component alloys, Mater Chem Phys 132(2-3) (2012) 233-238.
[40] A. Takeuchi, A. Inoue, Classification of Bulk Metallic Glasses by Atomic Size Difference, Heat of Mixing and Period of Constituent Elements and Its Application to Characterization of the Main Alloying Element, Materials Transactions 46(12) (2006) 2817-2829.
[41] N. Yurchenko, N. Stepanov, G. Salishchev, Laves-phase formation criterion for high-entropy alloys, Materials Science & Technology 33 (1) (2016) 17-22.
[42] B.D. Dunlap, P.J. Viccaro, G.K. Shenoy, Structural relationships in rare earth-transition metal hydrides ☆, Journal of The Less-Common Metals 74(1) (1980) 75-79.
[43] Y. Dong, Y. Lu, L. Jiang, T. Wang, T. Li, Effects of electro-negativity on the stability of topologically close-packed phase in high entropy alloys, Intermetallics 52(4) (2014) 105-109.

[44] A.K. Singh, N. Kumar, A. Dwivedi, A. Subramaniam, A geometrical parameter for the formation of disordered solid solutions in multi-component alloys, Intermetallics 53 (2014) 112-119.
[45] Y. Zhao, I.C. Choi, Y.J. Kim, J.I. Jang, On the nanomechanical characteristics of thermally-treated alloy 690: Grain boundaries versus grain interior, J Alloy Compd 582 (2014) 141-145.
[46] S. Ogata, J. Li, N. Hirosaki, Y. Shibutani, S. Yip, Ideal shear strain of metals and ceramics, Physical Review B Condensed Matter 70(10) (2004) 2516-2528.
[47] K.L. Johnson, Contact Mechanics, Journal of Tribology 108(4) (1985) 464.
[48] L. Wang, H. Bei, T.L. Li, Y.F. Gao, E.P. George, T.G. Nieh, Determining the activation energies and slip systems for dislocation nucleation in body-centered cubic Mo and face-centered cubic Ni single crystals, Scripta Mater 65(3) (2011) 179-182.
[49] Y.X. Ye, Z.P. Lu, T.G. Nieh, Dislocation nucleation during nanoindentation in a body-centered cubic TiZrHfNb high-entropy alloy, Scripta Mater 130 (2017) 64-68.
[50] D. Catoor, Y.F. Gao, J. Geng, M.J.N.V. Prasad, E.G. Herbert, K.S. Kumar, G.M. Pharr, E.P. George, Incipient plasticity and deformation mechanisms in single-crystal Mg during spherical nanoindentation, Acta Materialia 61(8) (2013) 2953-2965.
[51] J.K. Mason, A.C. Lund, C.A. Schuh, Determining the activation energy and volume for the onset of plasticity during nanoindentation, Physical Review B Condensed Matter 73(5) (2006) 054102.
[52] R.L. Fleischer, Substitutional solution hardening, Acta Metallurgica 11(3) (1963) 203-209.
[53] W.D. Nix, H. Gao, Indentation size effects in crystalline materials: A law for strain gradient plasticity, Journal of the Mechanics and Physics of Solids 46(3) (1998) 411-425.

Figure 1. (a) XRD patterns of $CoCrFeNiY_x$ HEAs, (b) Detailed scans for the peak of $(111)_{FCC}$, (c) Lattice parameters of the FCC phase as a function of the RE element Y content.

Figure 2. SEM images of the as-cast $CoCrFeNiY_x$ HEAs. (a) x = 0, (b) x = 0.05, (c) x = 0.1, (d) x = 0.2, and (e) x = 0.3. (f) The volume fraction of FCC and HS phases.

Figure 3. SEM image and EDS maps of the alloy elements of Co, Cr, Fe, Ni, and Y for the $Y_{0.1}$ HEA.

Figure 4. (a) TEM micrograph of the $Y_{0.1}$ alloy; SAED patterns corresponding to FCC phase (b) and HS1 phase (c).

Figure 5. (a) The typical nanoindentation *P-h* curves within the FCC phase and HS1 phase of the $Y_{0.2}$ alloy. (b) The average nanohardness on different phases of $CoCrFeNiY_x$ HEAs. (c) The average Young's modulus on different phases of $CoCrFeNiY_x$ HEAs.

Figure 6. (a) A typical first pop-in event at the beginning of the *P-h* curves of the FCC phase and HS1 phase obtained with nanoindentation. (b) Average reduced modulus and the maximum shear stress on the FCC phase and HS1 phase of the $Y_{0.2}$ alloy.

Figure 7. Vickers hardness as a function of the volume fraction of HS phase for the $CoCrFeNiY_x$ HEAs.

Figure 8. (a) Tensile engineering stress-strain curves of the $CoCrFeNiY_x$ HEAs. The insert is the schematic sample from the cross section of the specimen. (b) Compressive engineering stress–strain curves of the $CoCrFeNiY_x$ HEAs. (c) The nearly linear relationship between σ_y and V_{HS} for the $CoCrFeNiY_x$ HEAs.

Figure 9. The fracture surface morphology of the (a) Y_0 alloy, (b) and (c) $Y_{0.05}$ alloy, (d) $Y_{0.1}$ alloy, (e) $Y_{0.2}$ alloy, and (f) $Y_{0.3}$ alloy.

Table 1 Mixing enthalpy of different atom pairs, ΔH_{AB}^{mix} (kJ/mol), in the $CoCrFeNiY_x$ HEAs calculated by Miedema's approach [40].

Element (Melting point, Atomic radius)	Y	Co	Cr	Fe	Ni
Y (1,526 ℃, 180 pm)	—	-22	11	-1	-31
Co (1,495 ℃, 125 pm)	—	—	-4	-1	0
Cr (1,907 ℃, 128 pm)	—	—	—	-1	-7
Fe (1,538 ℃, 126 pm)	—	—	—	—	-2
Ni (1,455 ℃, 124 pm)	—	—	—	—	—

Table 2. Phase compositions (at.%) and crystal structures of different phases in the $CoCrFeNiY_x$ HEAs.

Alloys	Regions	Crystal structure	Chemical compositions (at.%)				
			Co	Cr	Fe	Ni	Y
Y_0	—	FCC	25.30	25.03	24.91	24.76	0
$Y_{0.05}$	DR	FCC	25.61	25.95	25.83	22.58	0.03
	ID	HS1	18.26	12.24	15.28	40.13	14.10
$Y_{0.1}$	DR	FCC	27.44	26.27	25.23	20.44	0.12
	ID	HS1	19.71	16.18	18.2	32.85	12.07
$Y_{0.2}$	DR	FCC	28.25	27.35	26.12	18.06	0.22
	ID	HS1	21.04	13.42	17.44	34.35	13.76
$Y_{0.3}$	DR	FCC	25.60	30.80	28.09	15.18	0.33
	ID	HS1	21.74	15.04	19.12	30.28	13.02
		HS2	18.19	8.81	13.17	42.64	17.19

Table 3 Summary of compression yield strength, σ_y, fracture strength, σ_f, and plastic strain, ε_p, of the CoCrFeNiY$_x$ HEAs

Alloys	σ_y (MPa)	σ_f (MPa)	ε_p (%)
Y_0	202	Not fractured	＞ 60
$Y_{0.05}$	563	2,175	33.5
$Y_{0.1}$	885	2,102	27.1
$Y_{0.2}$	1,286	1,694	7.3
$Y_{0.3}$	1,440	1,605	2.3

Table 4 Calculated parameters ΔS_{mix}, ΔH_{mix}, Ω, δ, VEC, $\Delta\chi$, and Λ for the studied CoCrFeNiY$_x$ HEAs.

Alloys	ΔS_{mix} (J/mol/K)	ΔH_{mix} (kJ/mol)	Ω	δ (%)	VEC	$\Delta\chi$	Λ
Y_0	11.526	-3.752	5.753	1.176	8.25	0.0967	8.334
$Y_{0.05}$	11.936	-4.181	5.342	4.879	8.185	0.1169	0.501
$Y_{0.1}$	12.198	-4.592	4.967	6.685	8.123	0.1330	0.273
$Y_{0.2}$	12.568	-5.351	4.388	9.073	8.000	0.1588	0.153
$Y_{0.3}$	12.825	-6.036	3.966	10.726	7.884	0.1791	0.111

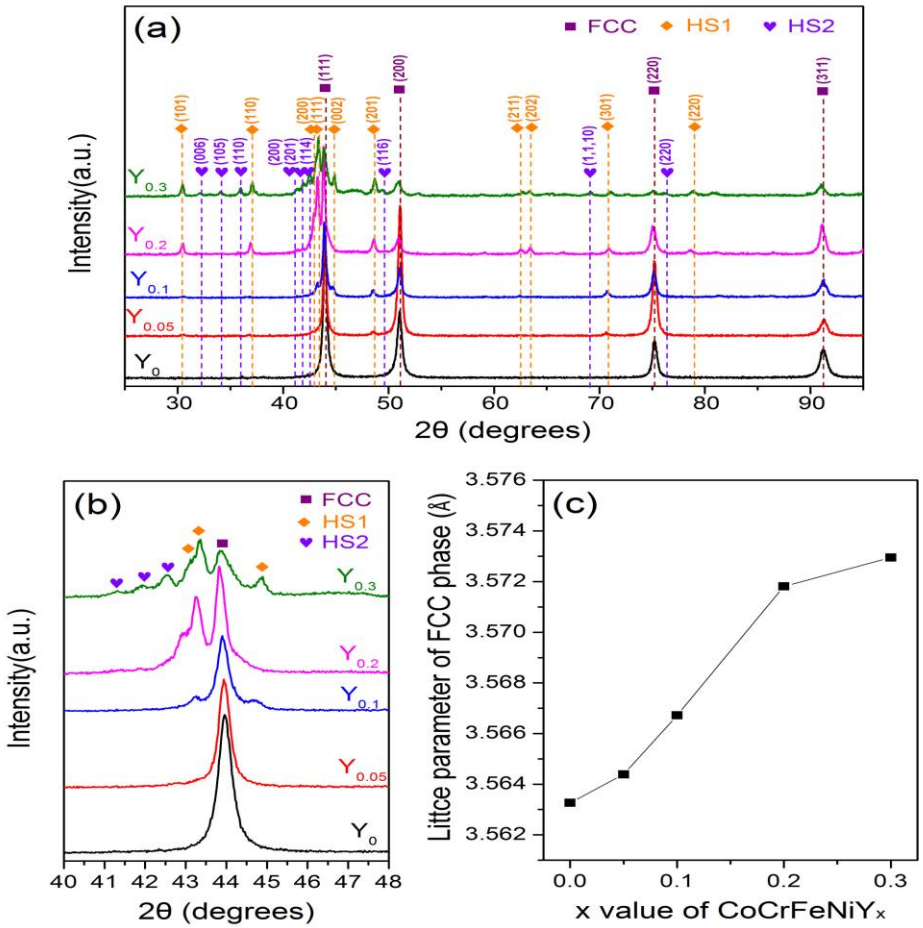

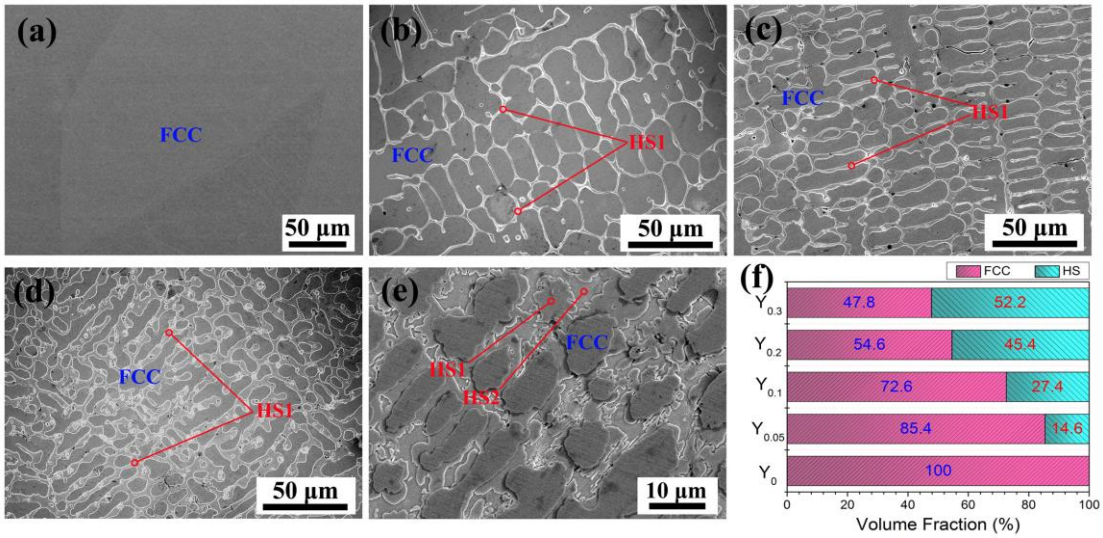
(a)
FCC
50 μm
(b)
FCC
HS1
50 μm
(c)
FCC
HS1
50 μm
(d)
FCC
HS1
50 μm
(e)
HS1
HS2
FCC
10 μm
(f)
FCC
HS
47.8
52.2
54.6
45.4
72.6
27.4
85.4
14.6
100
Volume Fraction (%)

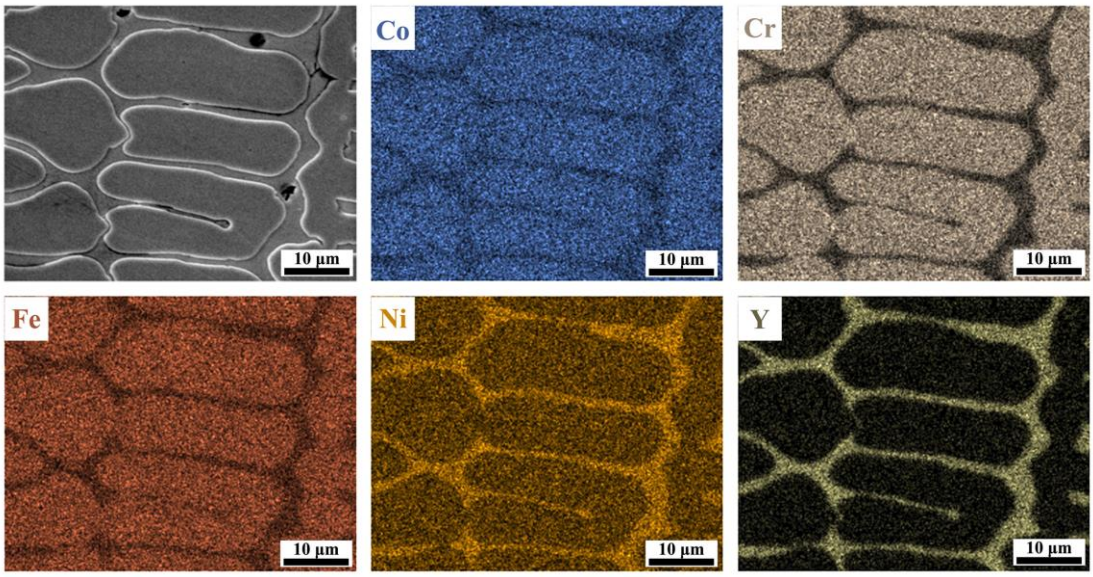
10 μm
Co
Cr
Fe
Ni
Y

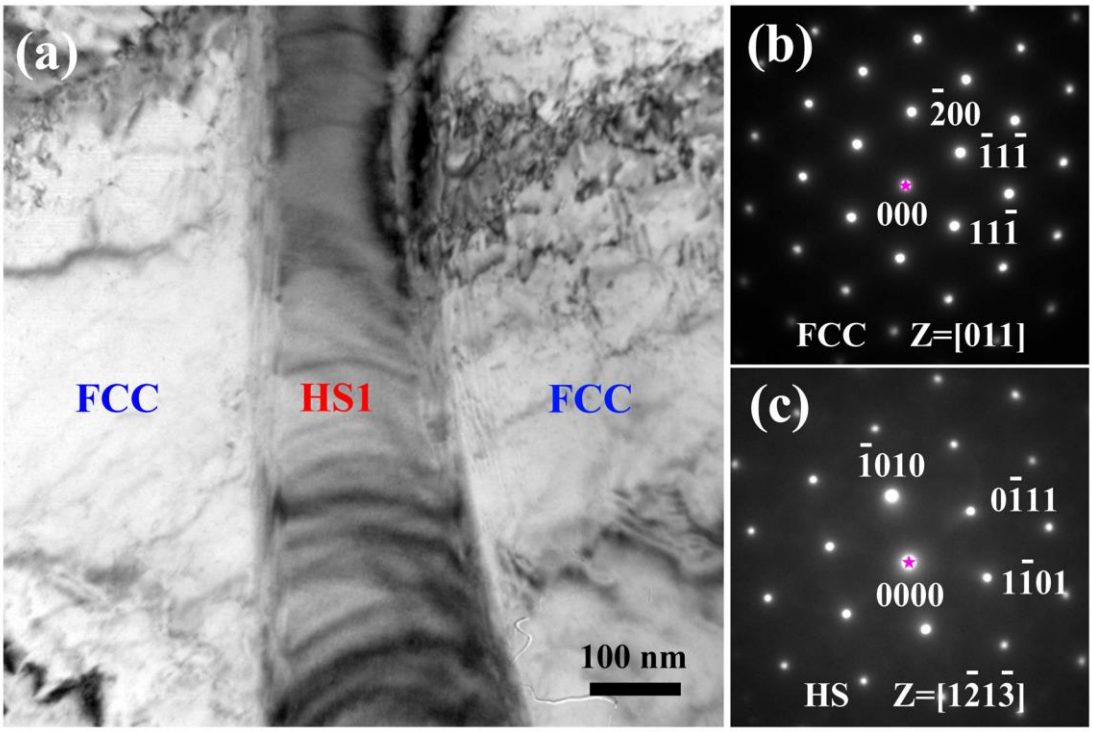

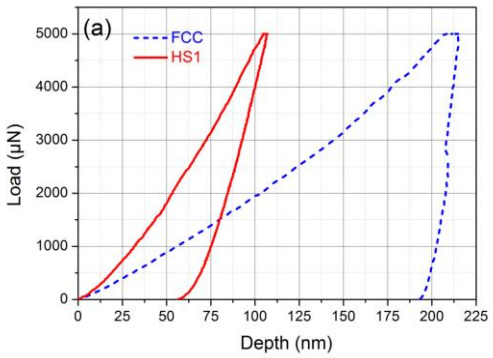

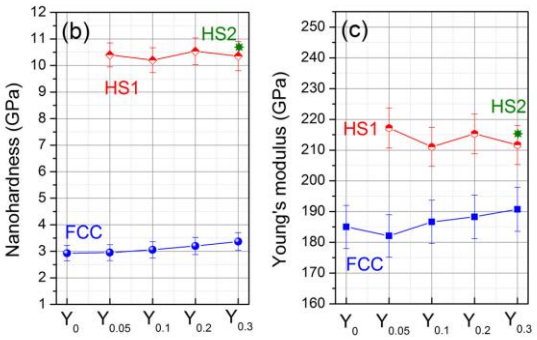

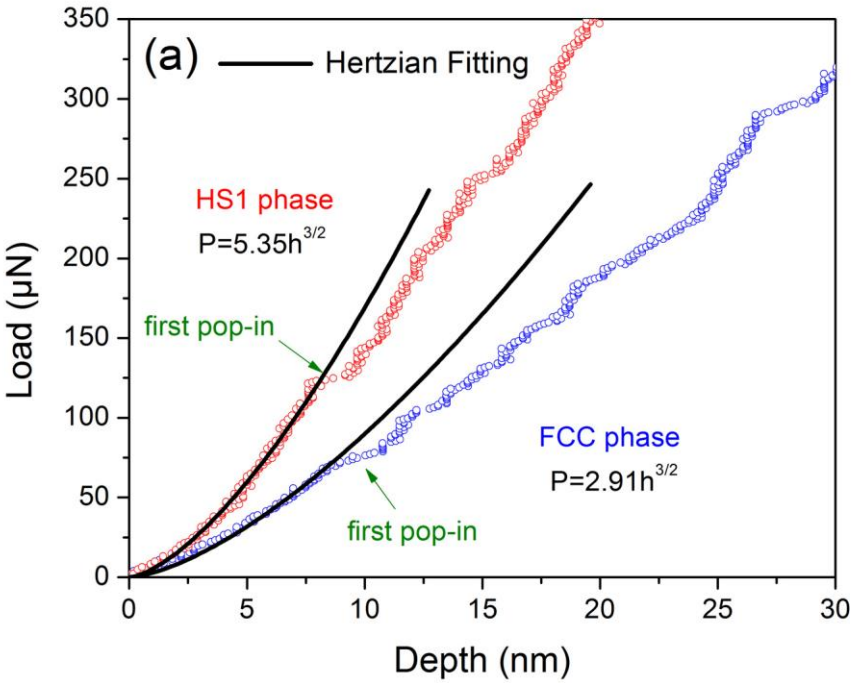
(a)
Hertzian Fitting
HS1 phase
P=5.35h^3/2
first pop-in
FCC phase
P=2.91h^3/2
first pop-in
Load (μN)
Depth (nm)
0
50
100
150
200
250
300
350
0
5
10
15
20
25
30

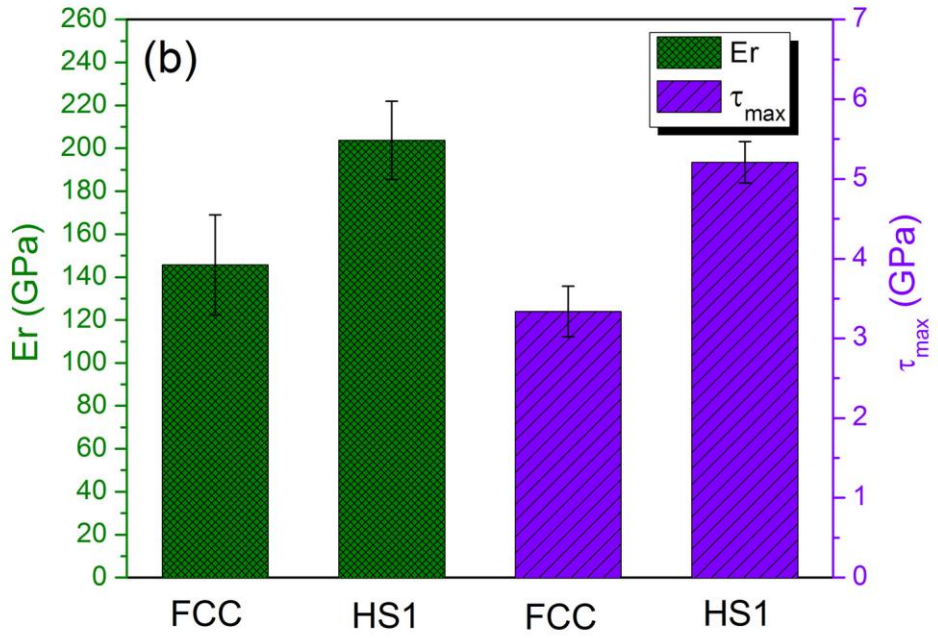
(b)
Er
τmax
Er (GPa)
τmax (GPa)
0
20
40
60
80
100
120
140
160
180
200
220
240
260
0
1
2
3
4
5
6
7
FCC
HS1
FCC
HS1

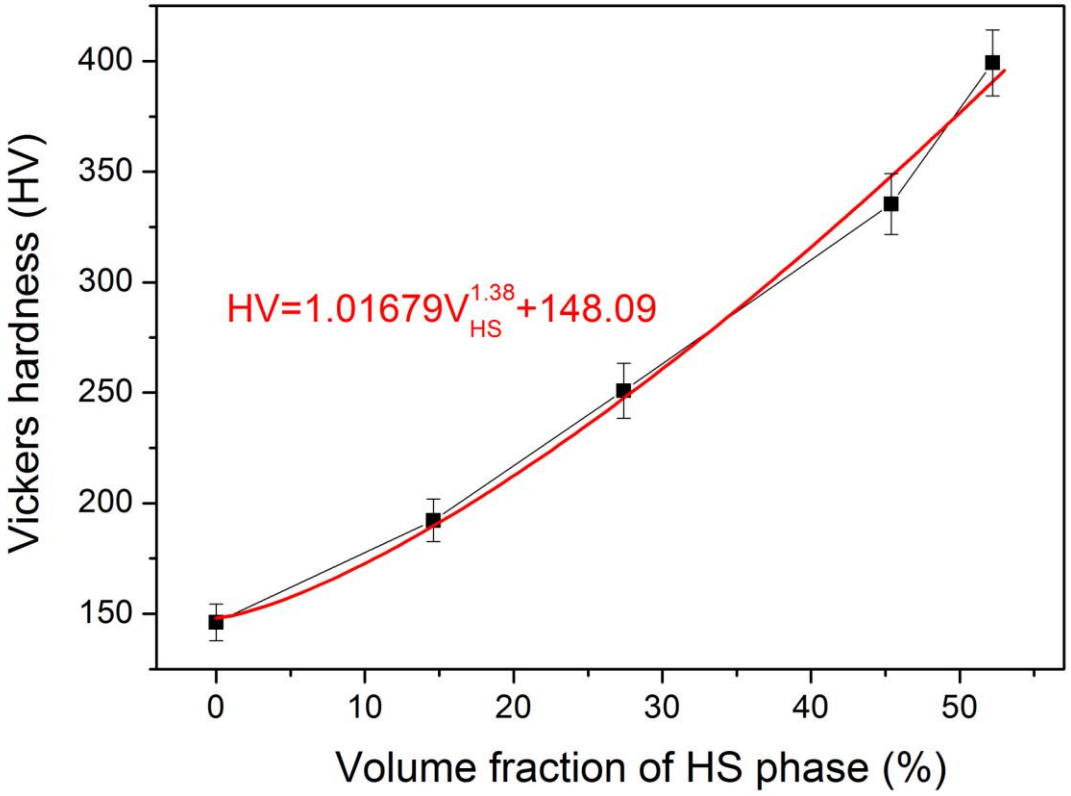

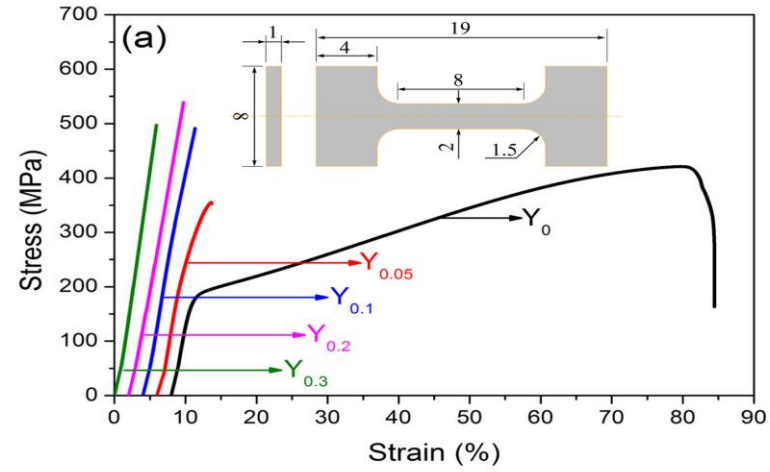
(a)
Stress (MPa)
Strain (%)
1
4
19
8
8
2
1.5
Y0
Y0.05
Y0.1
Y0.2
Y0.3

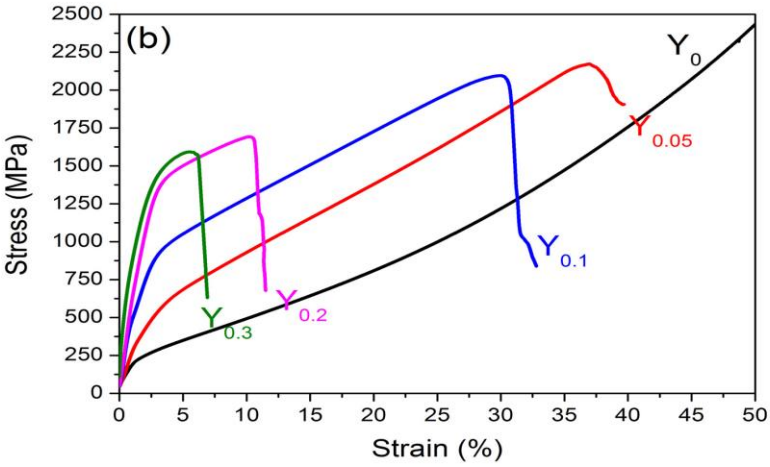
(b)
Stress (MPa)
Strain (%)
Y0
Y0.05
Y0.1
Y0.2
Y0.3

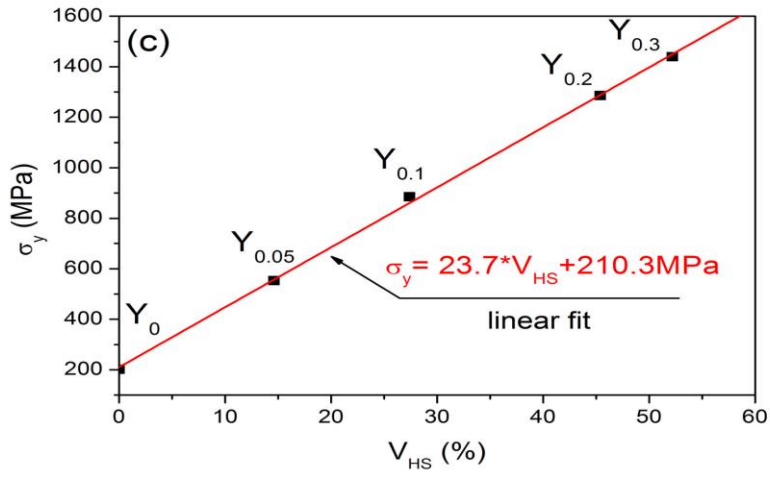
(c)
σy (MPa)
VHS (%)
Y0
Y0.05
Y0.1
Y0.2
Y0.3
σy = 23.7*VHS+210.3MPa
linear fit